Journal of The Electrochemical Society

The Electrochemical Society
Advancing solid state & electrochemical science & technology

OPEN ACCESS

The Role of Benzotriazole in Electrodeposition of $Cu_{1-x}Ni_x$ Alloys (0.05 < x < 0.15) on Cu and Ni Substrates

To cite this article: Karel P. S. Haesevoets *et al* 2022 *J. Electrochem. Soc.* **169** 052502

View the article online for updates and enhancements.

Investigate your battery materials under defined force!
The new PAT-Cell-Force, especially suitable for solid-state electrolytes!

- Battery test cell for force adjustment and measurement, 0 to 1500 Newton (0-5.9 MPa at 18mm electrode diameter)
- Additional monitoring of gas pressure and temperature

www.el-cell.com +49 (0) 40 79012 737 sales@el-cell.com

EL-CELL®
electrochemical test equipment

This content was downloaded from IP address 146.103.254.11 on 28/06/2022 at 14:38

Journal of The Electrochemical Society, 2022 **169** 052502

The Role of Benzotriazole in Electrodeposition of $Cu_{1-x}Ni_x$ Alloys (0.05 < x < 0.15) on Cu and Ni Substrates

Karel P. S. Haesevoets,[1,2] Harold G.G. Philipsen,[2] and Philippe M. Vereecken[1,2,z]

[1]*Centre for Membrane Separations, Adsorption, Catalysis, and Spectroscopy for Sustainable Solutions (cMACS), Department of Microbial and Molecular Systems (M^2S), KU Leuven-University of Leuven, Celestijnenlaan 200 F, box 2454, B-3001 Leuven, Belgium*
[2]*Imec, Kapeldreef 75, B-3001 Leuven, Belgium*

We investigated the benzotriazole enabled growth of low Ni content (5–15 at.%) CuNi alloy deposits by characterisation of its morphology and elemental composition as a function of substrate metal (Cu and Ni), charge density, current density, and potential-time response measured during electrodeposition. Alloy deposition starts in favor of Cu, forming a Cu-rich *layer* on a Ni substrate and Cu-rich *islands* on a Cu substrate after which aggregates only form on a Cu substrate, due to the ability of benzotriazole (BTAH) to chemically bond to Cu but not to a Ni surface. Furthermore, Ni deposits preferably on grain boundaries, BTAH gets incorporated in the deposit and forms a thin layer between the Cu substrate and the alloy deposit. Based on our findings a growth model for BTAH enabled CuNi growth is proposed which describes that the BTAH working mechanism is twofold. First, the additive shifts the onset potential of Cu^{2+} reduction closer to the Ni^{2+} reduction potential by forming a chemisorbed BTAH layer, thereby enabling Cu and Ni co-deposition and, secondly, during deposition it specifically interacts with Cu, thus inhibiting Cu dendrite formation.
© 2022 The Author(s). Published on behalf of The Electrochemical Society by IOP Publishing Limited. This is an open access article distributed under the terms of the Creative Commons Attribution 4.0 License (CC BY, http://creativecommons.org/licenses/by/4.0/), which permits unrestricted reuse of the work in any medium, provided the original work is properly cited. [DOI: 10.1149/1945-7111/ac35fa]

Manuscript submitted July 7, 2021; revised manuscript received October 8, 2021. Published May 5, 2022.

Supplementary material for this article is available online

The future of stacked integrated circuits (SICs) relies on the development of improved chip-to-chip solder connections.[1–3] The base for these so called "microbumps" is currently Cu but dissolution of the solder material (Sn) results in the undesired formation of Cu_3Sn and Cu_6Sn_5 intermetallic compounds with voids at the Cu and Cu_3Sn interface,[4–8] leading to electrical contact failure and physical degradation of the microbump.[9–13] This becomes even more detrimental when scaling down microbump dimensions, as voids remain of the same size. Introduction of 5 to 15 at.% Ni into the Cu base is expected to prevent Cu_3Sn formation in favour of the more stable $(Cu,Ni)_6Sn_5$, the growth of which is self-limiting and should not result in voids.[14]

The preferred method for electrodepositing CuNi alloys is galvanostatic deposition, i.e., using a controlled current. For co-deposition of metals which have a large difference in standard potentials (the value for Cu^{2+} to Cu^0 reduction is 0.59 V more *positive* than for Ni^{2+} to Ni^0),[15–17] alloy composition control is typically achieved by adding a complexant for the most noble metal (in this case Cu) which shifts the reduction onset closer to the other metal. However, when Cu reduction is under diffusion control, dendritic growth occurs (Fig. 1A). Although (sodium) citrate is well known to function as complexant and suppresses dendritic growth,[18–21] it is not compatible with the photoresist used during SIC manufacturing.

In previous work we developed a method for CuNi co-deposition on Cu substrates using benzotriazole (BTAH; Fig. 2A),[22] a well-studied corrosion inhibitor for Cu.[23,24] The additive shifts the reduction onset potential of Cu close to that of Ni, and avoids dendritic growth of Cu. It is well documented that BTAH chemisorbs to metallic Cu as well as its oxides.[24–26] There has been a lot of discussion in the literature on the type of interaction, possible chain forming and the orientation of the BTAH molecule to the Cu surface.[27–30] Grillo et al. examined the initial stages of benzotriazole adsorption on Cu and demonstrated that both perpendicular and parallel orientations of BTAH (Figs. 2B and 2C) occur on single-crystalline Cu(111) surfaces in ultra-high vacuum.[25,26] Compared to *metallic* Cu, BTAH chemisorbs faster and forms thicker layers on *oxidized* Cu surfaces.[31–34] There is no strong evidence in literature that BTAH will bond to metallic nor oxidized Ni. Cao et al. stated that "*BTAH may interact with the nickel surface as neutral molecules in the whole potential range*."[35] As the interaction of BTAH with Cu and Ni is so different, a detailed understanding of its impact on the alloy deposition process, composition, and morphology is crucial. From our previous research we know that BTAH mediated CuNi deposition on Cu yields hemispherical features which do not fully coalesce.[22] Figures 1B and 1C show well distributed CuNi aggregates which differ in size and number. As there is no adequate model for the development of such a morphology, the present work focusses on this. More specifically, we want to establish a growth model for galvanostatic deposition of CuNi alloys with a Ni content between 5 and 15 at.%, using an all-sulphate bath containing BTAH.

A systematic investigation of the number, size, and shape of the aggregates in the deposit and its elemental composition as a function of substrate metal (Cu, Ni), current density and charge density is performed. Finally, the depth resolved composition of the CuNi layer is examined by evaluating cross-sections of the deposit with TEM and EDS to determine the different phases during BTAH mediated CuNi growth.

Experimental

The standard solution composition used in this work ("CuNi+BTAH bath") is composed of 500 ppm 1H-benzotriazole (Acros Organics, 99%), 0.076 M $CuSO_4$ (Sigma Aldrich, powder, pentahydrate, 99.99%), 1.141 M $NiSO_4$ (Alfa Aesar, powder, hexahydrate, ACS, 98.0%), 50 ppm KCl (Merck, for analysis EMSURE, ACS), 0.485 M H_3BO_3 (Alfa Aesar, ACS grade, 99.5%) and pH was brought to 1.75 using 1.8×10^{-2} M H_2SO_4 (KMG, 96%). Boric acid was used to prevent passivation of electrodeposited Ni.[36–39] Variations on this bath are the "Cu+BTAH" and "Ni+BTAH" baths which have identical concentrations as for the CuNi+BTAH bath, however, $NiSO_4$ and $CuSO_4$ are, respectively, absent. An overview of all bath compositions used in this study can be found in Table I. For experiments where a 75 nm Cu strike was applied, it was deposited directly from the CuNi+BTAH bath at -0.125 mA cm^{-2}. The sample remained in the bath between completing the strike and initiating the experiment.

[z]E-mail: philippe.vereecken@imec.be

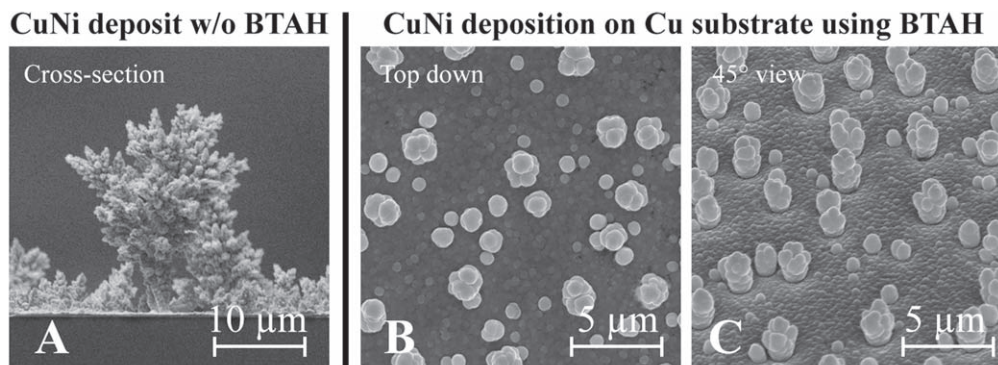

Figure 1. (A) Cross-section SEM image of CuNi deposited without BTAH. (B) Top down and (C) 45° tilted perspective SEM images of a CuNi layer deposited using BTAH, showing aggregates, deposited on a Cu substrate using 500 ppm BTAH at -31.2 mA cm^{-2} ($\omega = 100$ RPM).

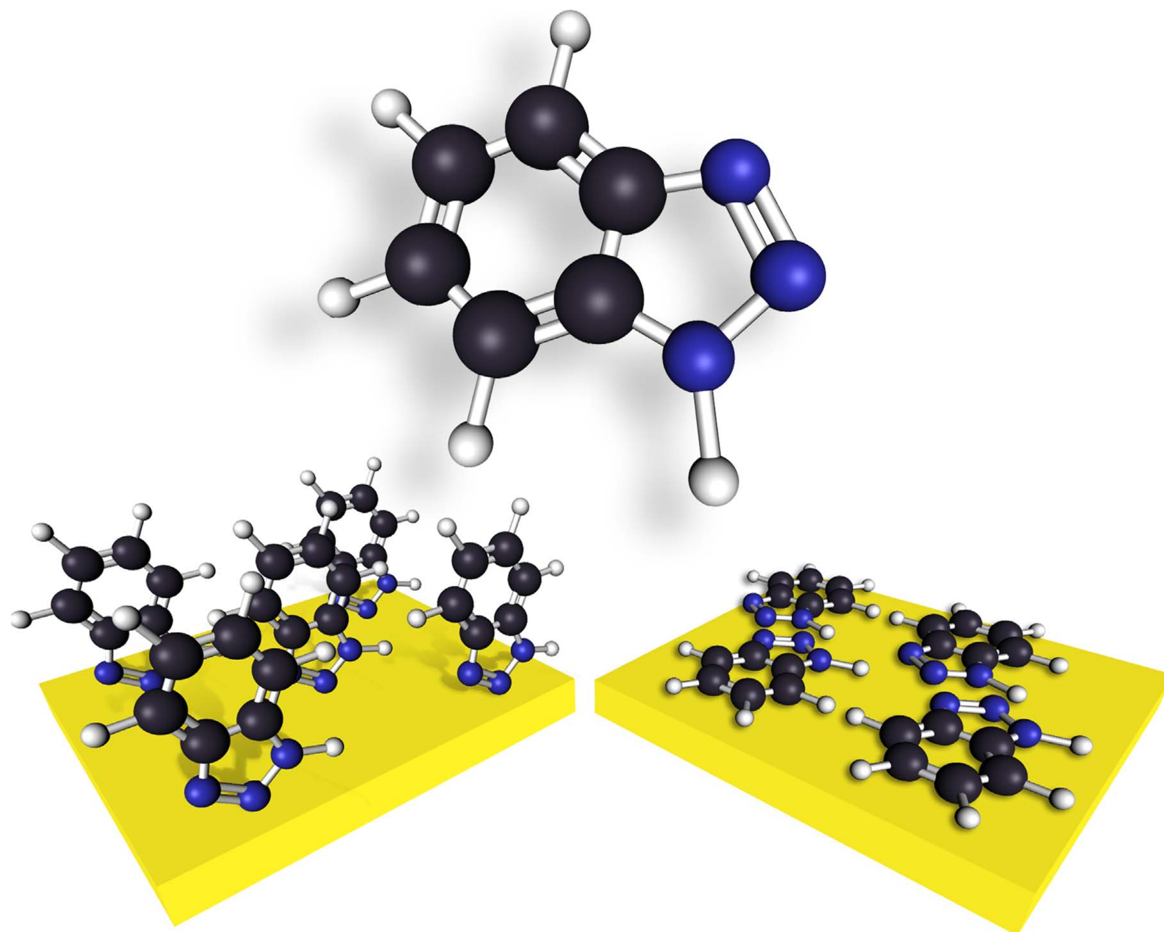

Figure 2. (A) Sketch representation of the BTAH structure, (B) perpendicular and (C) parallel orientation of BTAH on a Cu substrate.

Cu blanket thin films were produced on 300 mm diameter, 775 μm thick Si wafers. A stack of 150 nm Cu | 30 nm TiW was deposited by physical vapor deposition (PVD) on 50 nm SiN. Native oxide on Cu was removed by exposing the samples for 120 s to glacial acetic acid (Merck, anhydrous for analysis EMSURE, ACS) after which the samples were rinsed with water (18.2 MΩ·cm). Ni substrates were produced by depositing 150 nm Ni directly on the Cu substrate, using electrochemical deposition (ECD). The native oxide on Ni, in standard ambient temperature and pressure (SATP), typically has a self-limiting thickness of only 0.8 nm (2 to 3 monolayers of NiO),[40–44] whereas a native Cu oxide at room temperature has a thickness between 2 and 4 nm after an hour and between 4 and 8 nm after a month of air exposure.[45,46] Several cleaning routines were investigated to remove the small amount of Ni oxide, but no differences were registered in morphology, roughness or $U(t)$-transients. To limit the number of sample handling steps, only a water rinse was used for cleaning the Ni substrates.

Figure 3 shows the experimental setup. Experiments were performed at 45 °C to prevent boric acid from crystallizing. Blanket coupons (18 × 18 mm) were placed inside a rotating sample holder. Cu tape around the corners of the coupons provided electrical contact from the conductor in the sample holder to the front side of the coupon. To minimize the formation and movement of H_2 bubbles over the active surface during deposition, a circular hole (Ø 4 mm) in PTFE tape, created using a medical biopsy punch, defined the exposed area.

Table I. Electrolytes used in this work. In the coded names (A to G) Cu corresponds to the presence of $CuSO_4$, Ni to $NiSO_4$, BA to Boric Acid and BTAH to 1H-Benzotriazole.

		Bath compositions with component concentrations in mol L^{-1}					
		$[CuSO_4]$	$[NiSO_4]$	[KCl]	$[H_2SO_4]$[a]	$[H_3BO_3]$	[BTAH][b]
A.	$CuSO_4$ only	0.076		1.0×10^{-3}	1.8×10^{-2}		
B.	Cu + H_3BO_3	0.076		1.0×10^{-3}	1.8×10^{-2}	0.728	
C.	Cu+BTAH	0.076		1.0×10^{-3}	1.8×10^{-2}	0.728	0.0042
D.	Ni+BTAH		1.141	1.0×10^{-3}	1.8×10^{-2}	0.728	0.0042
E.	CuNi	0.076	1.141	1.0×10^{-3}	1.8×10^{-2}		
F.	CuNi+H_3BO_3	0.076	1.141	1.0×10^{-3}	1.8×10^{-2}	0.728	
G.	CuNi+BTAH	0.076	1.141	1.0×10^{-3}	1.8×10^{-2}	0.728	0.0042

a) The H_2SO_4 concentration of 1.8×10^{-2} mol L^{-1} corresponds to a pH of 1.75 in the described baths. b) 0.0042 mol L^{-1} BTAH corresponds to 500 ppm.

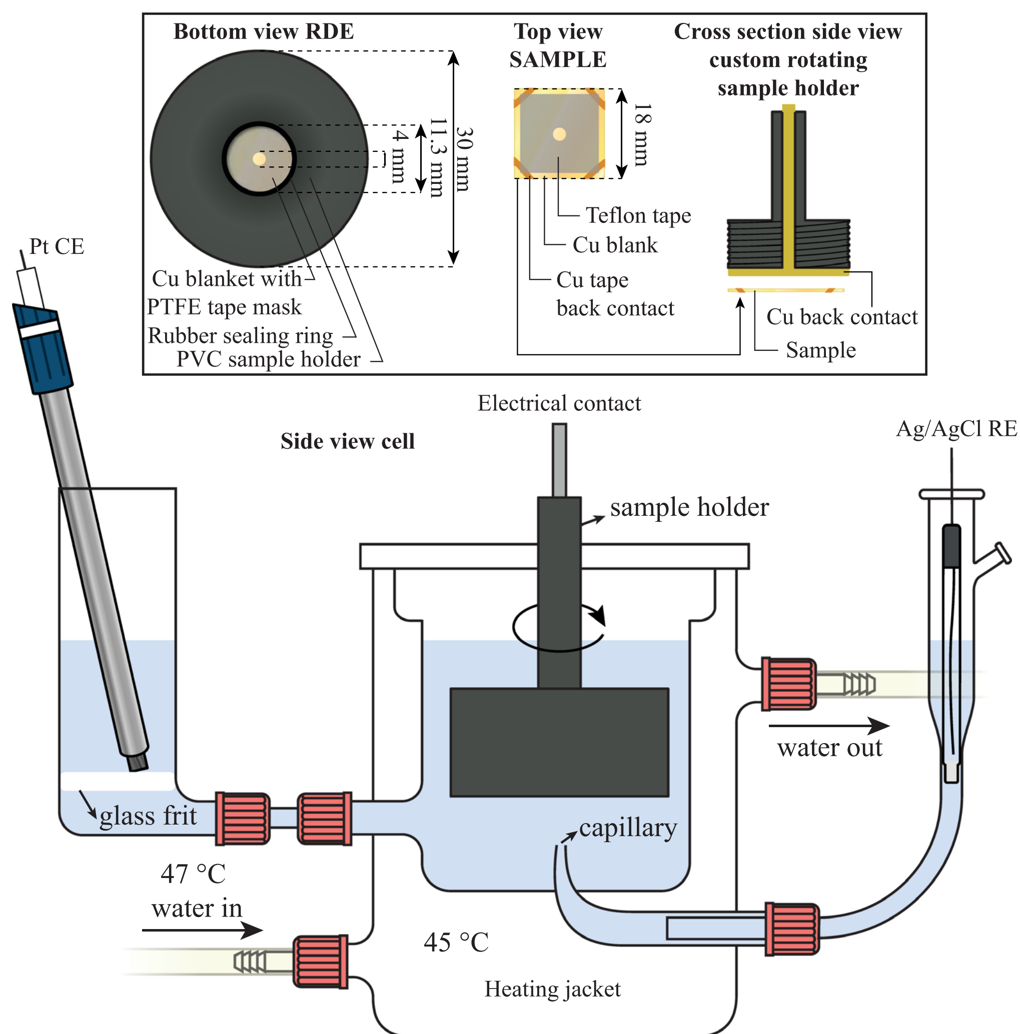

Figure 3. Schematic cross-section view of the RDE setup. The inset shows the bottom view of the rotating sample holder with the exposed surface of the removable Cu substrate.

A rotor (Radiometer) was used to control hydrodynamics (ω = 100 RPM). It was connected to a potentiostat (Parstat 4000, Princeton Applied Research), controlling the electrochemical measurements. Potentials were measured vs Ag/AgCl reference electrode (BASi MF-2052) and converted to relate to the standard hydrogen electrode (SHE; $U_{SHE} = U_{Ag/AgCl} - 0.205$ V). Correction for iR-drop was performed by the built-in software function. The counter electrode was a 25 mm^2 Pt plate (Radiometer Analytical M241Pt Metal Electrode).

The morphology and elemental composition of the deposits were examined using scanning electron microscopy (SEM; Fei Nova NanoSEM) and energy-dispersive X-ray spectroscopy (EDS; Oxford Instruments INCA Pentafet x3 mounted on the Nova NanoSEM). SEM images were taken using a 15 kV accelerating voltage and SEM-EDS measurements were performed top-down and averaged over a 2500 nm^2 surface area. When using SEM—EDS to determine alloy composition, one must consider that the method has a substantial interaction volume which reaches typically a depth of

0.5 μm in Cu at an acceleration voltage of 15 kV. Limited Monte Carlo simulations were performed (not shown) which showed that less than 0.1% of electron trajectories penetrated deeper than 0.5 μm into the metal.[47–49] As all considered deposits form a closed layer of at least 0.5 μm thick an overestimation of the Cu content due to probing of both the CuNi deposit and the Cu or Ni seed layer is not expected.

The "equivalent thicknesses" mentioned in this study refer to the calculated theoretical thickness of a cylindrical deposit in a circular open area based on the total charge consumed during deposition, assuming 100% current efficiency, a density of 8.96 g cm^{-1} for Cu and CuNi, 8.90 g cm^{-1} for Ni, and atomic weights of 63.55 g mol^{-1} for Cu and 58.69 g mol^{-1} for Ni.[50] The total amount of charge used is constantly monitored by the potentiostat during the experiment. No measured thicknesses are reported because the morphology of the deposits are not smooth enough to determine a single definite value and we found that the calculated equivalent thicknesses approach the mean thickness of a deposit, determined from cross-section SEM, well.

The evaluation of large aggregates is based on top-down and 45° angle view SEM images. Due to the irregular shape of these aggregates, automated evaluation was unreliable and, therefore, assessment was performed by hand. For cross-section analysis, a focused ion beam (FIB; Helios450HP dual beam SEM/FIB using a 30 keV Ga^+ ion beam) was used to cut 50 nm thick slices from the samples. The top surface of the samples was protected from possible FIB preparation damage by a spin-on-carbon (SOC) capping layer, which required a short 150 °C bake. The sections were then examined using high angle annular dark field scanning transmission electron microscopy (HAADF-STEM; FEI Tecnai F30 at 300 kV) and TEM-EDS (EDAX mounted on FEI Tecnai F30).

Results and Discussion

First, the composition of CuNi deposits on Cu and Ni substrates was evaluated as function of current density and charge density. The Cu:Ni ratio was quantified using SEM-EDS, having the advantage of a fast feedback which is beneficial during process optimization. This showed the target current density necessary for depositing CuNi in a 9:1 ratio from our electrolyte and it demonstrated the stability of this composition for variations in current density or charge density. Next, the difference in morphology between CuNi deposits on Cu and on Ni substrates was investigated. Per substrate the morphology was evaluated as a function of charge- and current density. Cross-sections of deposits on Cu and Ni substrates were studied using TEM-EDS, from which both the local alloy composition and morphology were investigated. The changes in elemental composition as a function of depth were correlated to the $U(t)$-transients measured during deposition. These transients were then used to compose the steady-state voltammograms. Finally, all observations were related to formulate a growth model.

Deposit composition as a function current density and charge density.—Films with a target thickness of 1 μm (equivalent film thickness using −2.72 C cm^{-2}, assuming 100% current efficiency) were deposited on blanket copper and nickel seed layers from the CuNi+BTAH bath (pH = 1.75) for varying current densities between −10 mA cm^{-2} and −55 mA cm^{-2} at a rotation rate of 100 RPM.

Figure 4A shows the Ni content of the deposits as a function of current density analyzed by SEM-EDS. No significant difference was observed between films deposited on Cu and Ni substrates. At current densities of −20 mA cm^{-2} and lower, the measured Ni content is below 1 at.% or the detection limit. From −25.5 to −48.0 mA cm^{-2}, the Ni content increases gradually from 8 to 23 at.%. For the largest current density used (−53.0 mA cm^{-2}), the Ni content shows a sudden increase to 43 at.%. The results show that it is possible to control the Ni content between 5 and 15 at.%, when using a current density ranging from −25.5 to −36.0 mA cm^{-2}.

To study the variation of Ni content throughout film growth, deposits were made at charge densities between −0.27 and −4.08 C cm^{-2} (corresponding to equivalent film thicknesses of 0.1 and 1.5 μm). Figure 4B shows the Ni content as a function of charge density for three current densities (−20, −31 and −42 mA cm^{-2}). At −20.0 mA cm^{-2} no Ni was detected for charge densities below −4.08 C cm^{-2} (Ni content is 3.2 at.% for the highest charge density). For −31.2 and −42.2 mA cm^{-2} the Ni content increases from 4.4 to 15.3 at.% and from 5.3 to 18.8 at.%, respectively, for charge densities going from −0.27 to −4.08 C cm^{-2}. All depositions start with a low Ni content which gradually increases over time, but the rate decreases with time.

Effect of BTAH-substrate interaction on the alloy morphology.—Next, we compared the morphological difference between BTAH mediated CuNi growth on Cu and Ni substrates. Figure 5 shows SEM images of CuNi deposits on (A) Cu and (B) Ni substrates (−31.2 mA cm^{-2}, 1 μm thick at −2.72 C cm^{-2}). The difference between the two cases is apparent; for the Cu substrate, a large density of vertical or pillar-like "aggregates" appear with much smaller rounded particles or "granules" in-between whereas the Ni substrate was uniformly covered with these granules with only occasionally an isolated aggregate (see inset). This demonstrates that the morphology of a CuNi deposit from a BTAH-containing bath strongly depends on the substrate metal and thus the initial stages of nucleation and growth.

The number, height and shape of the CuNi aggregates were investigated as a function of charge density (i.e., deposition time/thickness) and current density to probe the interaction of BTAH with the substrate. Figure 6 shows the quantification of the aggregates in terms of number and height as a function of charge density. For these experiments, a CuNi deposit of 1 μm in thickness (−2.72 C cm^{-2}) with a ∼15 at.% Ni content obtained at −31.2 mA cm^{-2} was chosen (Fig. 4).

Figure 6A shows that on a Cu substrate, aggregates are present in large numbers (around 10^5 cm^{-2}), regardless of the charge density used. On a Ni substrate the number of aggregates always stays below 100 cm^{-2}. This indicates that they form in the nucleation phase and no new aggregates form afterwards.

Figure 6B shows the height of the aggregates, as determined from side-view SEM images, as a function of charge density. On a Cu substrate, their height increases linearly from 1 μm at −0.27 C cm^{-2} (i.e., about 10 times the equivalent film thickness) to 10 μm at −4.08 C cm^{-2} (i.e., about 7 times the equivalent film thickness). Hence, on a Cu substrate the majority of the current goes to the growth of the aggregates (more details will follow when discussing Fig. 9). On a Ni seed, the few existing aggregates do not seem to grow significantly over time and thus the current goes to the growth of the granules.

Figure 6C shows the four major aggregate shapes: nodular, elongated, branched and dendritic. These types are related to the height of the aggregates in Fig. 6B. The largest aggregates on the Ni substrates are of the nodular type. For deposition on Cu blankets, the shape of the aggregates develops with charge density from nodular at −0.27 C cm^{-2} to elongated and branched at −1.36 and −2.72 C cm^{-2} to dendritic at −4.08 C cm^{-2}.

On Cu, a large density of copper nodules is formed. These nodules grow about 10 times faster than the film in the field area. We suspect that the nodular growth starts at defects in the adsorbed BTAH layer on the pristine Cu substrate, where adsorption and diffusion of BTAH to the fresh copper is too slow, resulting in continued fast uninhibited growth of the nodule vs slower growth in the inhibited field. A similar mechanism was observed by Moffat et al.[51] where Cu deposition through a polyether layer resulted in Cu deposition at the defects in the polymer layer which led to a positive feedback mechanism that enabled localized growth of Cu. On Ni, few nodules are observed which do not grow faster than its surrounding field. Here, the effect is less pronounced as fresh copper

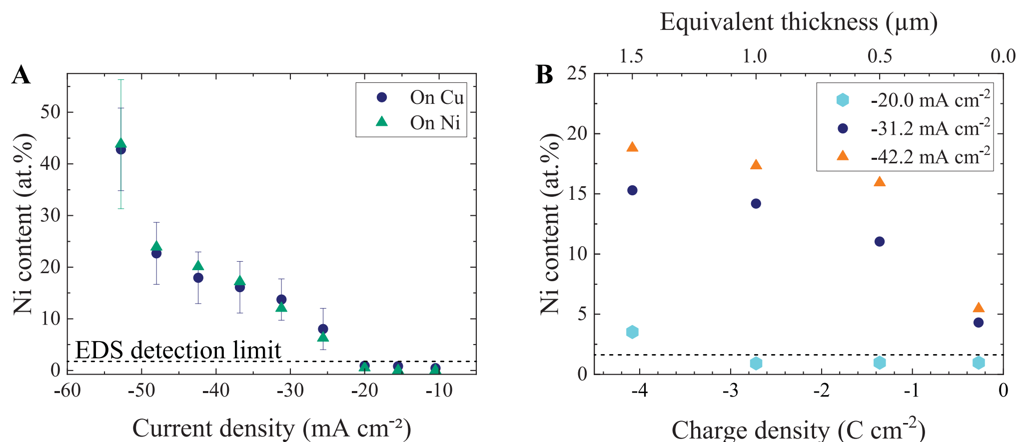

Figure 4. (A) SEM-EDS determined Ni content of 1 μm thick (-2.72 C cm^{-2}) CuNi deposits as function of deposition current density ($\omega = 100$ RPM) on (●) Cu and (▲) Ni substrates. The error bars are the result of measurements on at least 3 separate deposits. (B) SEM-EDS determined Ni content of CuNi deposits as a function of charge density on Cu substrates for depositions at (⬢) -20.0, (●) -31.2 and (▲) -42.2 mA cm^{-2} ($\omega = 100$ RPM).

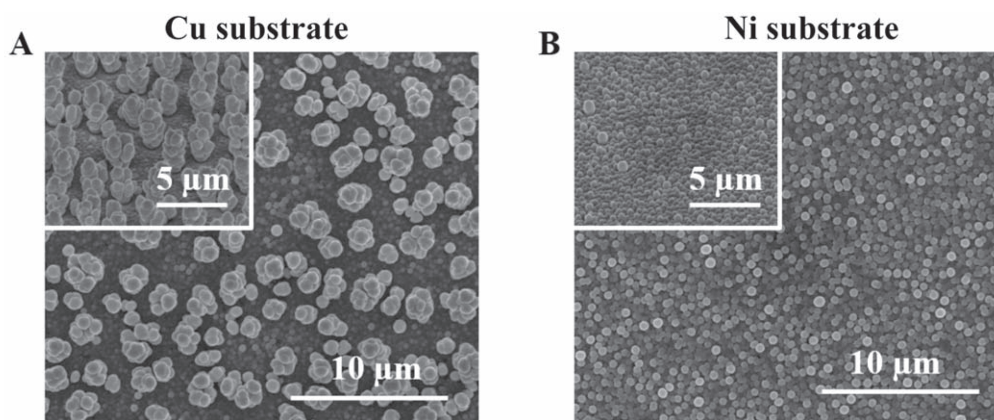

Figure 5. Top-down SEM images of 1 μm thick (-2.72 C cm^{-2}) CuNi deposited at -31.2 mA cm^{-2} on (A) Cu and (B) Ni substrates. The insets show 45° SEM views of the deposits. The Ni content for these samples is 14.2 at.% on Cu and 13.7 at.% on Ni. ($\omega = 100$ RPM).

surface in the field needs to be inhibited by BTAH and initial inhomogeneities which form these nodules are quickly reduced.

The impact of current density on the aggregates was studied in more detail for an equivalent film thickness of 1 μm (assuming -2.72 C cm^{-2} for 1 μm). The number of aggregates on Cu (Fig. 7A) stays in the 10^5 cm^{-2} range and their height varies between 5 and 6.5 μm (Fig. 7B). The shape of the aggregates transitions from elongated to branched when current densities over -25.5 mA cm^{-2} are applied (Fig. 7B). The number density of aggregates on Cu does not change significantly with current density—and their average height or thus the relative growth rate of nodule to film is similar for current densities between -20 and -50 mA cm^{-2}.

From all results shown in Figs. 6 and 7 it is concluded that aggregates form right from the start of deposition on a Cu substrate, they continuously grow, and their shape evolves as a function of time and is impacted by current density. The fact that the number of aggregates on a Ni substrate is substantially lower than on a Cu substrate (Fig. 6A) suggests that the strong interaction of BTAH with Cu is a key factor for aggregate growth. BTAH affects the CuNi deposition process in three ways: shift of the Cu^{2+} reduction onset potential,[22] the formation of a BTAH layer on the substrate (only on Cu; Fig. 6), and alleviate dendritical growth on Cu (Fig. 1).

While the elemental composition is not impacted by the substrate (Fig. 4), the morphologies differ on Cu and Ni (Fig. 5). When we compare the aggregate growth (Figs. 6 and 7) to the alloy composition (Fig. 4) there is no obvious relation with their number, height nor shape.

To determine the effect of the substrate and the differential BTAH inhibition on deposit morphology, three cases with different affinities for BTAH adsorption were investigated. In the first case, where little to no BTAH could adsorb to the substrate prior to the CuNi deposition (column 1 of Fig. 8), we studied morphologies on ECD Ni (Fig. 8A) and PVD Cu on which a Cu strike was electrodeposited (directly from the CuNi+BTAH bath at a potential for Cu deposition only and immediately followed by the CuNi alloy deposition; Fig. 8B). This way, BTAH does not have enough time to form a thicker adsorption layer on Cu as compared to when a Cu substrate is at rest in the solution prior to the initiation of CuNi electrodeposition. No aggregates were observed in this case. The deposit on the Cu strike resembles the deposit on Ni, confirming that a short Cu strike, without a time delay before depositing CuNi, is effective enough to prevent efficient BTAH adsorption to the substrate and thus results in an aggregate-free deposit.

The morphology from the first case was compared to deposits from the second case for which we know that BTAH will have a moderate interaction with the substrate (column 2 of Fig. 8). We used ECD Cu samples where the oxide was chemically removed (Fig. 8C) and ECD Cu with a Cu strike but this time with a 30 s delay between the strike and the start of CuNi deposition (Fig. 8D). The presence of aggregates in this second case is evident. The morphology of the deposit on the Cu strike with a 30 s delay before the CuNi deposition contains even more aggregates compared to the deposit on oxide free Cu (here the deposition started about 10 s after inserting the substrate in the electrolyte solution). The roughness of

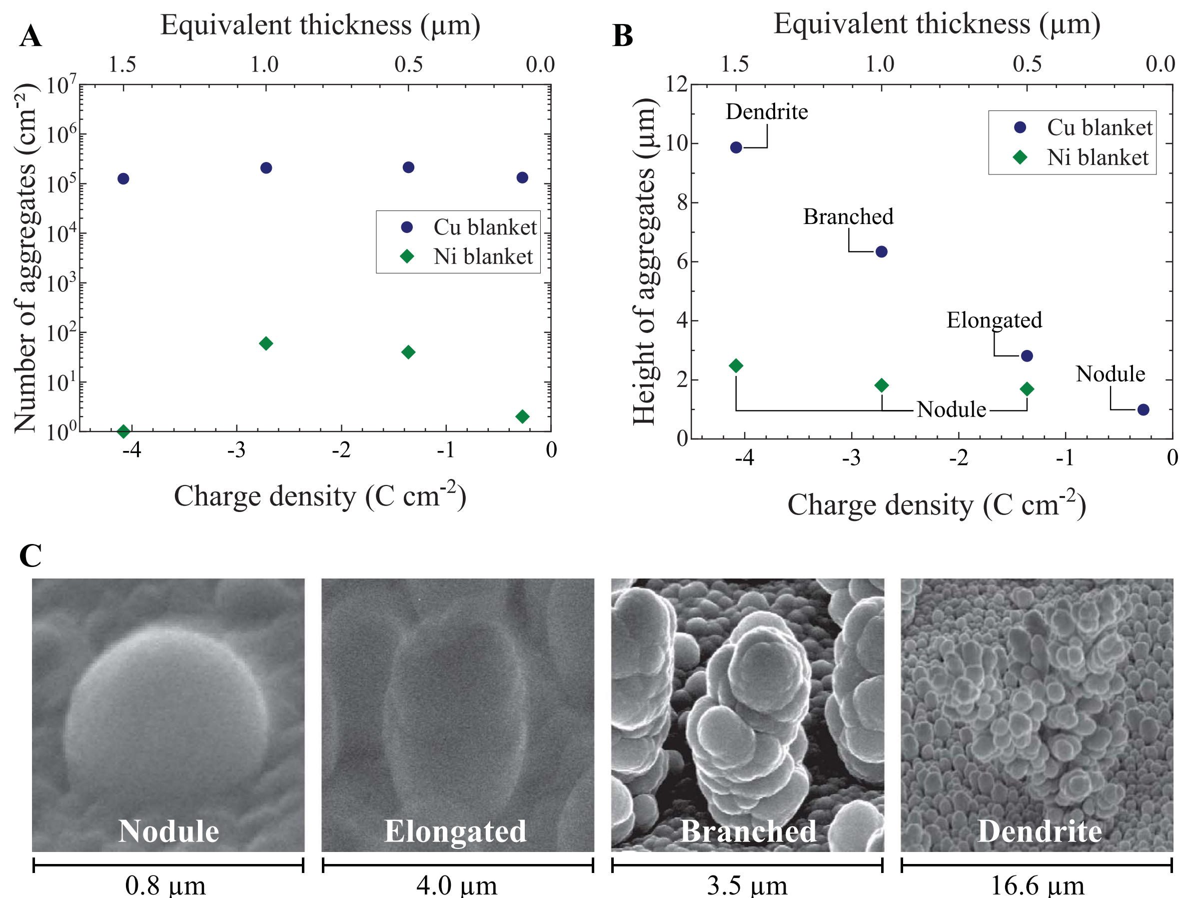

Figure 6. (A) Number and (B) height of aggregates of CuNi deposits as function of charge density, deposited at -31.2 mA cm^{-2} on a (⬤) Cu substrate and a (◆) Ni substrate (ω = 100 RPM). (C) 45° view SEM images of the four considered types of aggregate shapes, ranked from simple hemispheres or "nodules" to large complex dendrite-like features. A charge density of -2.72 C cm^{-2} and -2.92 C cm^{-2} correspond to a 1 μm film of dense Cu and dense Ni, respectively (note the logarithmic vertical scale).

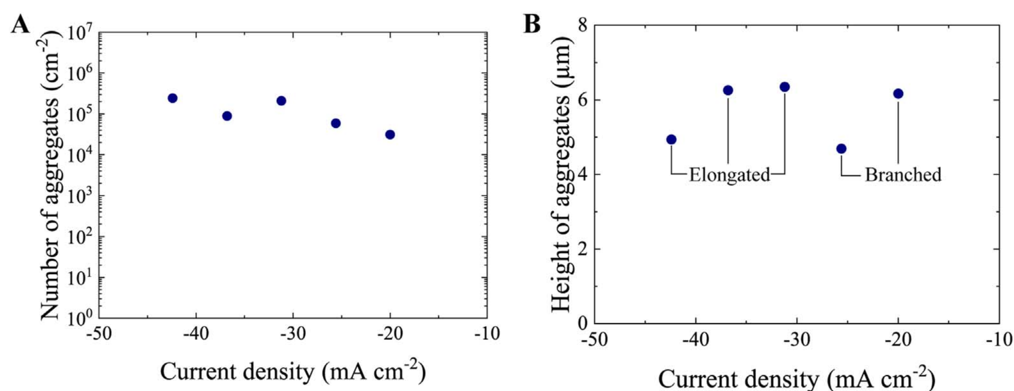

Figure 7. (A) Number, (B) height and shape type of aggregates of CuNi deposit as function of deposition current density on Cu substrates for 1 μm thick (-2.72 C cm^{-2}) CuNi deposits (ω = 100 RPM).

the deposit is, therefore, function of the time of interaction between BTAH and the substrate.

In the third case we investigated the morphologies of substrates with an elevated interaction with BTAH (column 3 of Fig. 8). The first Cu substrate was covered with native oxide. Where the previous Cu surfaces were all treated with glacial acetic acid to remove oxides and protect the surface from reoxidizing during transfer from the solution to the deposition bath, the current substrate was only rinsed with water after being exposed to open air for three months (Fig. 8E).[24–26] The second substrate is again an oxide free ECD Cu substrate but for this experiment we used a significantly higher BTAH concentration (+250 ppm or +50%; Fig. 8F). Looking at the oxidized Cu substrate in Fig. 8E, there is no longer any deposition in the field and only aggregates (height > 8 μm) are present. When the BTAH concentration is increased from 500 to 750 ppm, the deposit only consists out of a low number of very complex aggregates between 25 and 40 μm in height (Fig. 8F). Note that for all results shown in Fig. 8 the same amount of deposition charge was used.

For comparison, pure Cu and Ni were deposited from Cu+BTAH and Ni+BTAH baths, respectively, at -31.2 mA cm^{-2}, on both Cu and Ni substrates (not shown). Only the Cu deposit on Cu has large granules and aggregates. In contrast, the Ni deposit on Cu is smooth

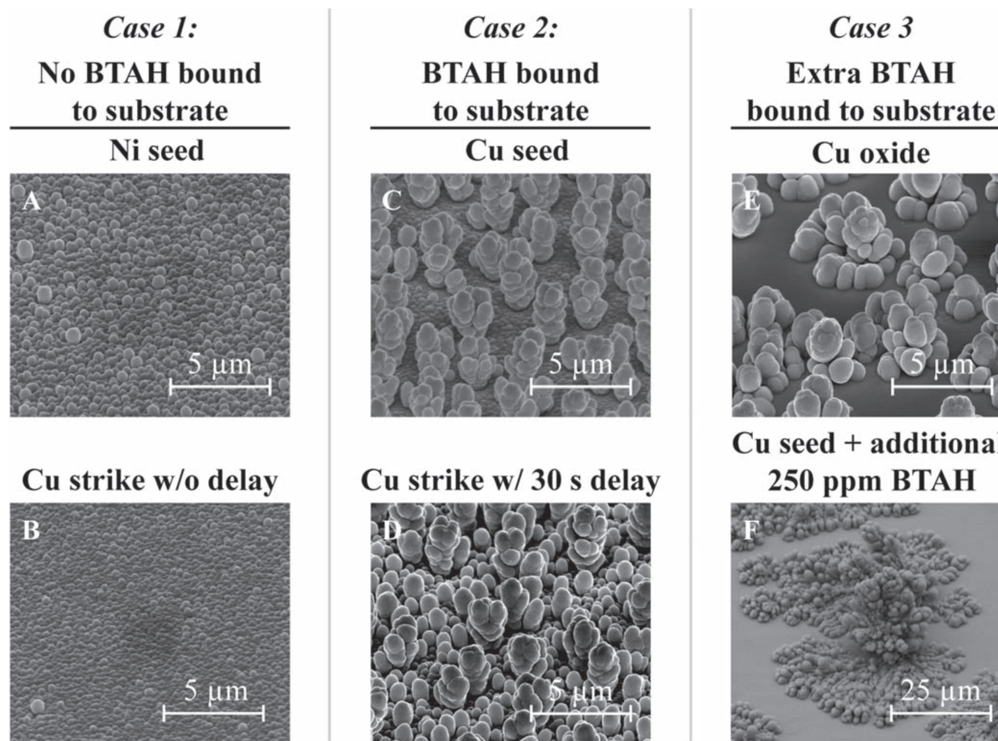

Figure 8. 45° SEM views of CuNi deposits when deposited on (A) Ni substrate, (B) 75 nm Cu strike without delay, (C) Cu substrate, (D) 75 nm Cu strike with 30 s delay, (E) Cu oxide, and (F) Cu substrate where an additional 250 ppm BTAH was added to the bath. All depositions were performed at -31.2 mA cm^{-2} and are 1 μm thick (-2.72 C cm^{-2}).

even though BTAH was present in the solution. Both Cu and Ni BTAH mediated depositions are smooth on Ni. From these observations we derive that no aggregates grow when BTAH is not bound to the substrate and the degree to which BTAH interacts with the surface determines how many and how large the aggregates grow. When BTAH is given no opportunity to form a substrate-bound layer (on Ni or directly after a Cu strike), no aggregates are formed. Confirmation can be found in the opposite extreme cases where BTAH bonds so well to the surface that deposition in the field is inhibited and only extreme aggregates occur. We suspect that the existing BTAH-substrate layer on the Cu substrate is disrupted by the Cu and Ni deposition reactions which results in the formation of aggregates at specific points on the surface where the current density is now significantly higher than intended.

Figure 9 shows TEM-EDS line scans (first column) and HAADF-STEM images (second column) of the FIB-cut cross-sections of the deposits on both Cu and Ni substrates. For the Cu substrate samples EDS color intensity mappings are shown in overlay with the HAADF-STEM images. The Cu seed sample used in the first two rows of Fig. 9 is the same as those shown in Fig. 5A. The Ni sample used here is the same as the one used in Fig. 5B. The HAADF-STEM image of Fig. 9B shows that CuNi grows in closely packed columns on the Cu seed. The EDX line scans of the deposits on Cu (Figs. 9A and 9C) show that the bottom of the deposit is significantly more Cu rich than the rest of the deposit. This Cu-rich area is also clearly visible as contrast difference at the bottom of the deposits in the HAADF-STEM images (Figs. 9B and 9D). On the Ni seed (Fig. 9F), the first 200 nm of the deposit forms a flat, yet somewhat porous layer, followed by alternating layers with different Cu:Ni ratios (indicated by the black/white bar). Up to ± 400 nm, the deposit remains flat whereafter the deposit becomes granular with spherical CuNi morphology.

EDS line scans and mappings show that, for the CuNi columns on Cu (Figs. 9A and 9B), two distinct zones with slightly increased Ni content (∼5 at.% compared to 3.5 at.% Ni) exist within the deposit. On Ni (Figs. 9E and 9F), above the Cu-rich porous layer, the Cu:Ni ratio alternates between 5 and 17 at.% in a 200 nm thick layered part of the deposit. In the granular top layer, the Cu:Ni ratio remains between 5 and 7 at.%. The EDS line scans also confirm that on Ni too the initial stages of the CuNi deposition are Cu rich. The observations show that CuNi deposition starts in favor of Cu, forming a Cu-rich layer on an ECD Ni substrate and Cu-rich islands on a PVD Cu substrate. The Ni content is not constant throughout the deposit, especially in the 200 to 400 nm range on Ni.

When we compare the TEM-EDS line scans and the elemental mappings of the columnar growth and the aggregate we determine that the analysed part of the aggregate (1.0 μm) relates well to the bottom 400 nm of the deposition in the field in terms of spatial elemental composition. Throughout the whole deposit the Ni content increases in two horizontally distinct zones within the deposit, both in the aggregate as well as in the columnar deposits. Both aggregates and columns share the same features and undergo the same variations during deposition which is a result of the former observation that the only difference between a column and an aggregate is the increased growth rate of the latter.

On the grain boundaries between neighboring granules (Fig. 9B), or at the point where a granule and an aggregate coalesce (Fig. 9D EDS), there is an increase in Ni content. It appears that Ni preferably deposits at the grain boundaries. The previously discussed Ni-rich zones within the deposit could be related to perturbances in the growth kinetics of the layer where a temporary reduced growth rate of the layer allows for an increased exposure time of the fresh grain boundary to Ni deposition.

We can use the EDS N signal as a "probe" for the presence of BTAH in the deposit as it is the only compound used containing nitrogen (3 atoms per molecule; see Fig. 2A). For the Cu seed (Figs. 9A and 9C), the line scans show a narrow BTAH-rich region above the PVD Cu film, which is present due to the strong interaction of BTAH with a Cu surface. This is not the case for the Ni seed (Fig. 9E) where the BTAH adsorption is non-existing (Fig. 9F). Therefore, at least part of the Cu substrate-bound BTAH layer remains intact while the CuNi deposit grows on top of it.

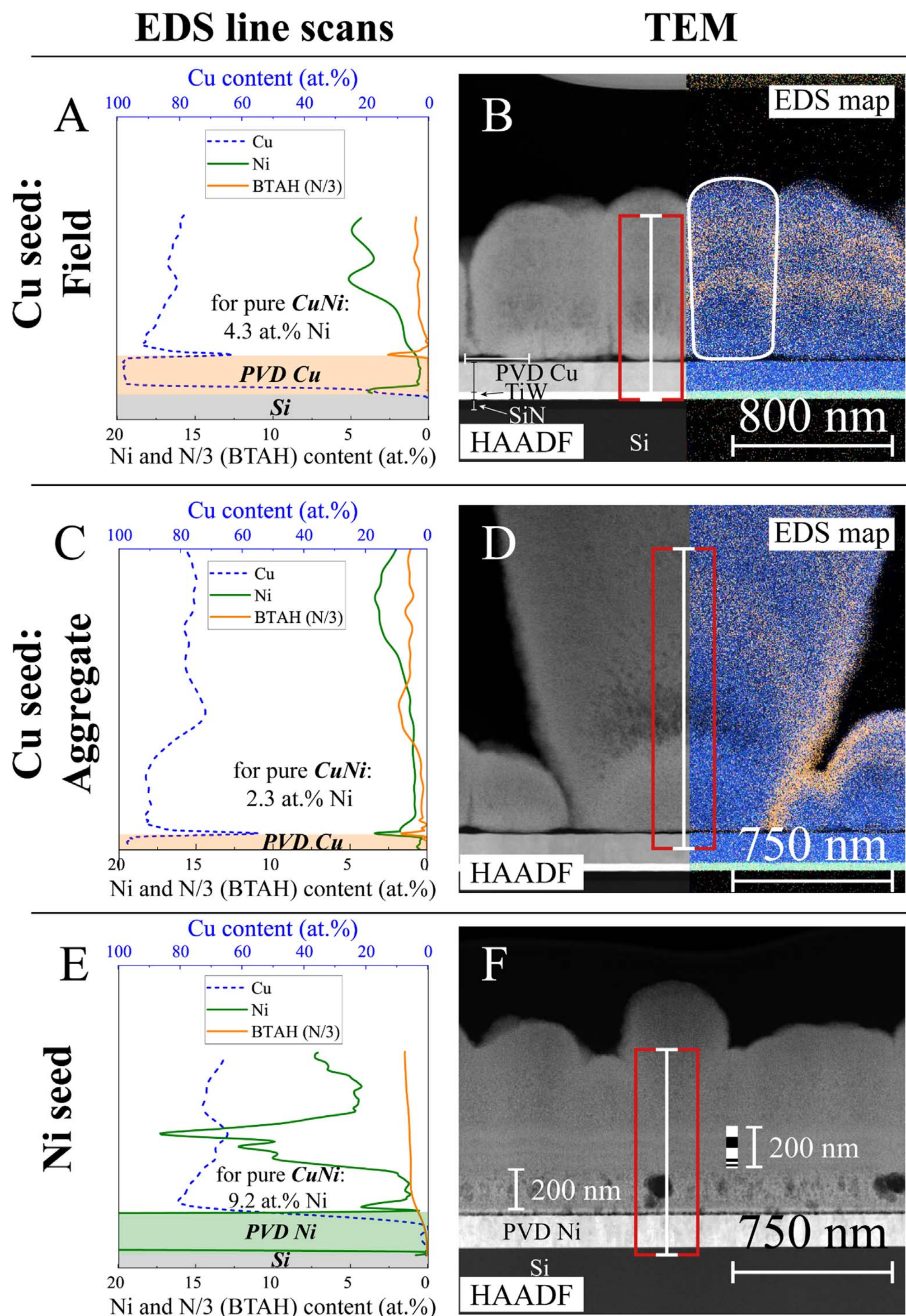

Figure 9. (A, C, E) TEM-EDS line scans of Cu (dashed blue), Ni (green), and N/3, as a single BTAH molecule contains 3 nitrogen atoms, to represent the incorporated amount of BTAH (orange) paired with the (B, D, F) HAADF-STEM cross-section images. For the cross-sections on Cu, EDS mappings are overlayed on the right side of the HAADF images. The results are ordered in the following rows: (A, B) CuNi columnar growth in the field on Cu, (C, D) detail of a CuNi aggregate on Cu and (E, F) CuNi deposit on Ni. The line scans for Cu are on a compressed scale (top axis) so that the features of the other line scans (bottom axis) remain legible. Depositions were performed at -31.2 mA cm^{-2} and are 1 μm thick (-2.72 C cm^{-2}). Exceptionally the Ni substrate is PVD Ni on Si rather than ECD Ni on Cu.

Although BTAH is incorporated throughout the whole deposit for both substrates, the amount of incorporation is significantly lower in the Cu-rich base of the deposit on Cu whereas on Ni the BTAH incorporation is uniform over the whole deposit. Just above the Cu-rich base of the aggregate (Fig. 9D), the TEM-EDS line scan shows increased BTAH incorporation. We argue that this is part of the initial BTAH layer which gets dislodged by a Cu is land that initiated at a defect in the layer, partially grows underneath it and subsequently gets encapsulated by the fast-growing aggregate.

Note that SEM-EDS measurements (Fig. 4) only take Cu and Ni into account, the scan is taken from above and is scanned over a wide area of 20 × 20 μm. TEM-EDS measurements, on the other hand, also include C and N, lowering both the Cu and Ni at.% and these measurements are very localized. When we discard the latter

two elements, we get a mean Ni content of only 4.3 at.% in the deposit on a Cu substrate (with a further decreased 2.3 at.% at the base of the aggregate) and 9.2 at.% on Ni. Because of the limited SEM-EDS penetration depth (~0.5 μm), the zone with significant increased Ni content on the Ni substrate, as measured with cross-section TEM-EDS (Fig. 9E), would not contribute that much to the SEM-EDS measured Ni content (Fig. 4). For our purpose, we are interested in the Cu:Ni ratio at the top of the deposit where the self-limiting $(Cu,Ni)_6Sn_5$ intermetallic phase will form. Complementary, TEM-EDS has the advantage that it can give insight into the *local* alloy composition and detect all 4 relevant elements (Cu, Ni, C, and N; detection limits are on the order of 1 at.%).

U(t)-responses of BTAH mediated CuNi depositions and steady-state voltammograms.—Next, we investigate the steady-state voltammograms and $U(t)$-transients of CuNi depositions on Cu and Ni to see if any previous observations can be correlated to changes in potential during deposition.

Steady-state voltammograms (SSV) for alloy deposition on Cu and Ni substrates were constructed from the steady-state potentials of all measured $U(t)$-responses (the complete set of corresponding $U(t)$-responses are collected in the supplementary material (supplementary Figure 1 available online at stacks.iop.org/JES/169/052502/mmedia) and a select overview is shown in Fig. 11). Figures 10A and 10B show SSVs of the CuNi+BTAH bath (■) for alloy deposition on Cu and Ni substrates, respectively. Additionally, SSVs were constructed for Cu+BTAH (●) and Ni+BTAH (▲) baths. For a Cu substrate in a Cu+BTAH bath, Cu^{2+} reduction has an onset potential of −0.36 V. The hydrogen evolution reaction (HER) starts at −0.56 V (onset marked with a blue diamond, ◆) where the current exceeds the copper diffusion limit of $-18.0\ mA\ cm^{-2}$ at 100 RPM as determined from an LSV without BTAH (see supplementary Figure 2). This way the onsets of HER and Cu^{2+} reduction are enough apart so that the limiting current density of the latter can be observed. It was demonstrated before that the addition of BTAH does not affect the limiting current of Cu^{2+} reduction.[22] For the CuNi+BTAH bath, the Cu^{2+} reduction onset is found to be −0.28 V and HER starts at −0.55 V. The copper deposition diffusion-limited current density is $-12.5\ mA\ cm^{-2}$ for CuNi+BTAH bath i.e., lower than for Cu+BTAH bath. From Fig. 4, we know that Ni deposition starts for $i < -20\ mA\ cm^{-2}$ or thus $U < -0.7$ V. Note that the exponential current increase after onset of HER is slower for the CuNi+BTAH bath than the Cu+BTAH bath. This difference is quantified by fitting the Butler-Volmer equation (kinetic limitation, see supplementary Fig. 2) to the data points where HER occurs, up to the point where Ni deposition starts, and using the resulting charge transfer coefficient, α, as a measure for the rate of current increase as function of overpotential. The limiting current for Cu deposition was set as the baseline for HER (i_{H_2} partial current is $0\ mA\ cm^{-2}$) For the Cu+BTAH bath α was 0.25 and 0.28 for the Cu and Ni substrates, respectively. Interestingly, for the baths containing $NiSO_4$ (CuNi+BTAH and Ni+BTAH baths) α was between 0.1 and 0.13. This demonstrates that the reduced HER kinetics is not related to the electrode material but to the presence of $NiSO_4$ in the solution.

Starting from a copper substrate, the onset of HER is around −0.55 V for all three baths. For a Ni substrate, the HER onset starts earlier at −0.50 V for the Ni+BTAH bath. This is in line with the lower hydrogen chemisorption energy per atom for Ni (−0.51 eV) than for Cu (−0.05 eV), resulting in easier formation of H_2 at the Ni electrode.[52] For the baths containing $CuSO_4$, HER on Ni starts at −0.57 V on Cu and −0.55 V on Ni after a small amount of Cu was already deposited. On both substrates, the onset potentials for Cu^{2+} (marked with a red circle, ●) in the CuNi+BTAH bath are lower (~0.6 V) than in the Cu+BTAH bath. This is due to a reduction in BTAH mediated Cu^{2+} onset shift when large quantities of $NiSO_4$ are present in the electrolyte.[22] $NiSO_4$ also reduces the (absolute) limiting current density of Cu^{2+} reduction for the CuNi+BTAH bath compared to the Cu+BTAH bath.[22]

For the Ni+BTAH bath, the whole LSV is shifted 0.06 V more negative on Cu than on Ni which can be attributed to the difference in substrate material (discussed above). The onsets of HER and Ni^{2+} reduction (onset marked with a green triangle, ▼) are −0.56 V and −0.83 V, respectively, on Cu and −0.50 and −0.77 V, respectively, on Ni. Note that the Ni^{2+} reduction reaction in all cases will be under kinetic control due to the high concentration of $NiSO_4$ (1.14 M). The Ni^{2+} onset in the CuNi+BTAH bath occurs at −0.73 V on both substrates where some Cu was deposited before Ni deposition started.

Figure 11 shows the first 10 s of the potential-time responses for depositions from CuNi+BTAH (A and B), Cu+BTAH (C and D) and Ni+BTAH (E and F) baths at current densities varying between −6.0 and $-62.5\ mA\ cm^{-2}$ on Cu and Ni substrates, respectively. The complete $U(t)$-responses are summarized in the supplementary Fig. 1.

In all Cu substrate cases, the electrode potential in the CuNi+BTAH bath (Fig. 11A) goes first to the copper deposition potential around −0.4 to −0.5 V (orange transient). When incrementally increasing the current density above that of the limiting current density for copper deposition, the potential subsequently goes first to

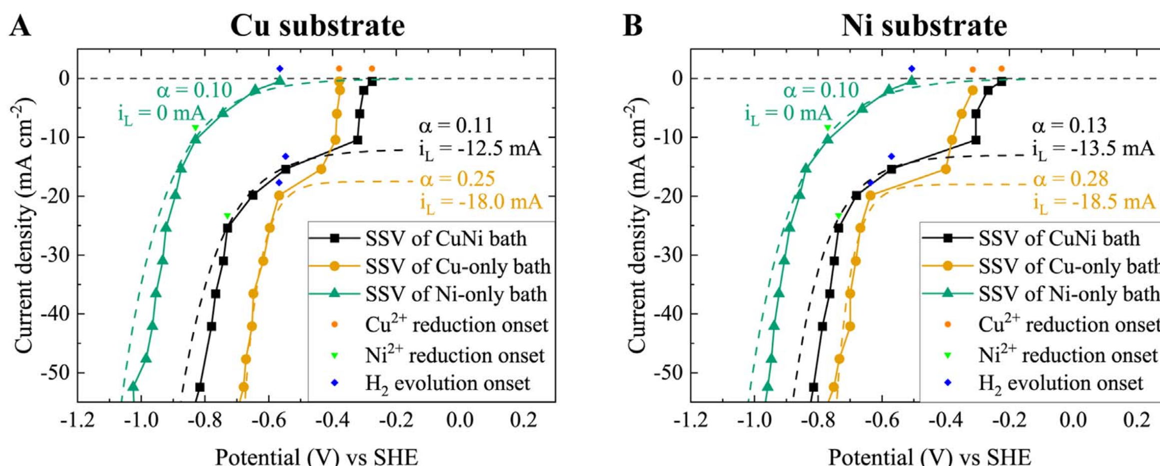

Figure 10. (A) Steady-state voltammograms for 1 μm thick deposits ($-2.72\ C\ cm^{-2}$) on Cu and (B) Ni rotating substrates (ω = 100 RPM) in a (■) CuNi+BTAH bath, (●) Cu+BTAH bath and (▲) Ni+BTAH bath. The onsets of Cu^{2+} reduction, HER and Ni^{2+} reduction are indicated as ●, ◆, and ▼, respectively. The Butler-Volmer equation was fitted (—) to each SSV so that the change in current density as function of overpotential for H_2 reduction could be quantified by the charge transfer coefficient (α). The limiting currents for Cu^{2+} reduction are labeled with "i_L" and were determined in LSVs (see supplementary material).

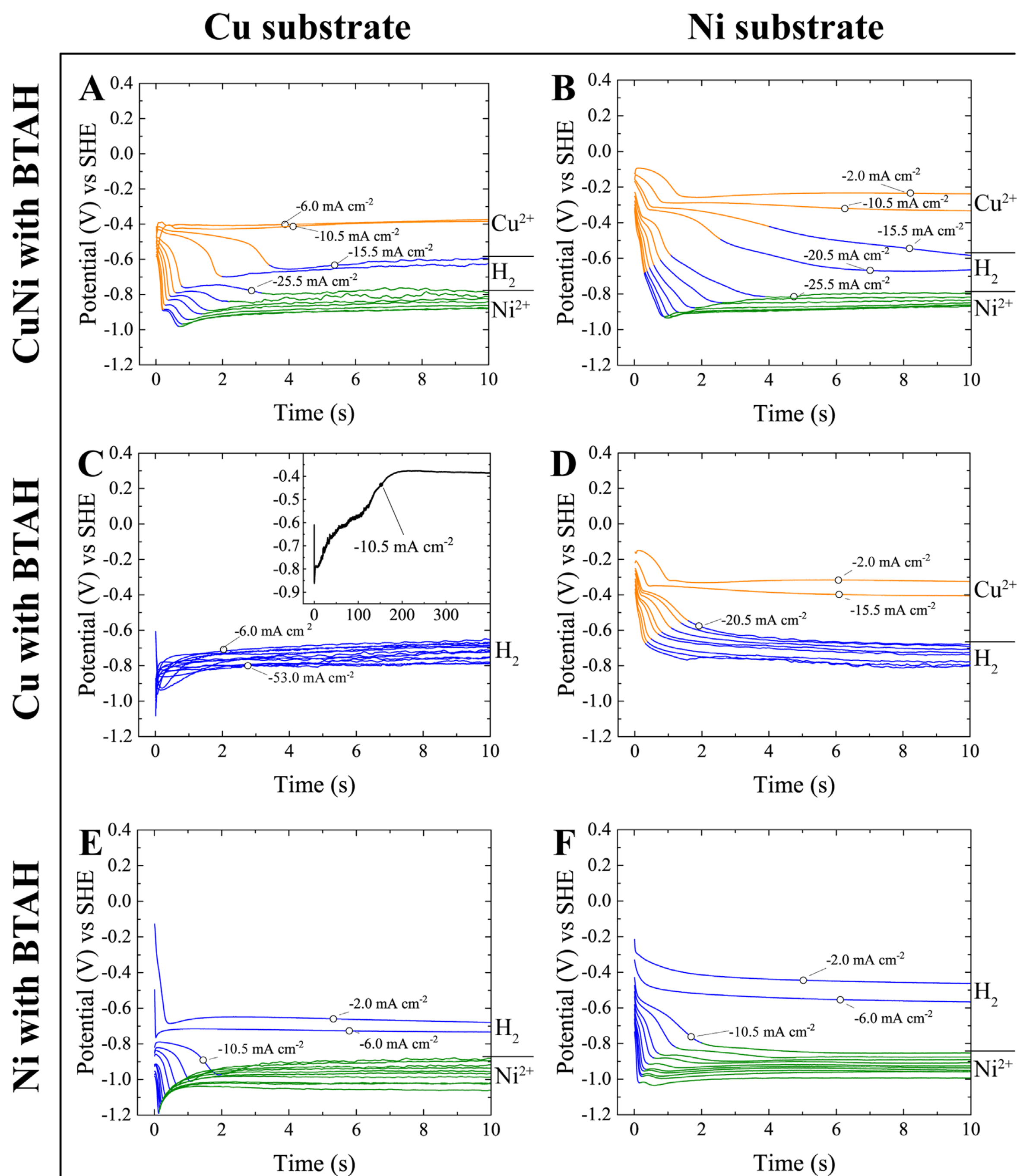

Figure 11. First 10 s of potential-time responses of depositions from (A, B) CuNi+BTAH, (C, D) Cu+BTAH and (E, F) Ni+BTAH baths on Cu and Ni substrates at different current densities. Orange parts of the transient indicate Cu^{2+} reduction, blue for HER and green for Ni^{2+} reduction. The potential differences between the three reduction reactions are well defined in the three indicated potential windows. The inset in figure C shows the full-time scale transient for Cu deposition on Cu from a Cu+BTAH bath at -10.5 mA cm^{-2}.

that for additional HER (blue transient) and then to that for additional Ni deposition (green transient) partial currents. The onset time of each additional partial current decreases with increasing cathodic current density (and the potential step increases). The steady-state potentials (reached > 7 s) form the SSVs of Fig. 10. The different reaction contributions were confirmed above by SEM-EDS.

On a Ni substrate, the electrode potential in the CuNi+BTAH bath (Fig. 11B) follows a similar stepwise potential transient behavior, except for an additional initial potential step (< 1 s) for the nucleation and growth of copper on the Ni substrate. As in this case BTAH can adsorb only *after* Cu is formed, the transients appear more sluggish. Indeed, as discussed above, the BTAH surface layer strongly affects the electrode kinetics of the different partial currents. The effect of BTAH becomes very evident for the transients in the Cu+BTAH bath (Figs. 11C and 11D). For the Cu substrate, the potential goes immediately to the HER (+ simultaneous Cu deposition), even for applied current densities below the Cu deposition diffusion limit. Because of the dense BTAH surface layer on a Cu substrate, the Cu^{2+} reduction onset is shifted outside the potential window of water, causing HER to occur from the initial stages of the deposition. On a longer timescale (inset in Fig. 11C), the BTAH surface layer becomes diluted as more fresh copper is deposited, and eventually disappears. As such, the copper deposition potential shifts again more positive than the HER onset potential. In

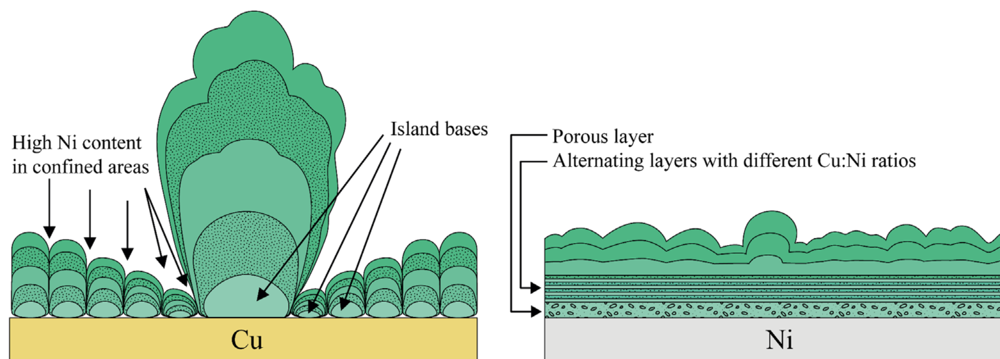

Figure 12. Schematic representation of the proposed growth model of BTAH mediated CuNi growth on (left) Cu and (right) Ni substrates.

the absence of BTAH this is obviously not the case (see supplementary Fig. 2). Interestingly, this polarization effect is also not present in the CuNi+BTAH bath (Figs. 11A and 11B) as the presence of large amounts of $NiSO_4$ reduce the effectiveness of BTAH to shift the Cu^{2+} reduction.[22] For the Ni substrate (Fig. 11D), the transient first goes to the copper deposition potential as first some copper needs to be deposited before BTAH adsorption can occur. However, the depositions at -6.0 and -15.5 mA cm^{-2}, i.e., below and close to the diffusion-limited current, both result in Cu only deposition. Hence, this steady-state situation corresponds more to the longer time transient where the initial dense BTAH surface layer got diluted ($t > 200$ s for $i = -10.5$ mA cm^{-2}).

Finally, for the Ni+BTAH bath the transient profiles are comparable for both substrates: on the Cu substrate the potentials are on average 0.1 V lower than on Ni which again can be attributed to the polarization effect of the BTAH surface layer on the Cu substrate. In the Ni+BTAH bath Ni starts depositing on both substrates at current densities above -10.5 mA cm^{-2}. Note that in all cases, the transients with HER showed some noise due to bubbles. The potential fluctuations became quite drastic after 25 s (see supplementary Fig. 1) as the H_2 bubbles got trapped on the sample surface in the downward-facing sample holder (see setup in Fig. 3).

Conclusions

We investigated the benzotriazole enabled growth of low Ni content (5–15 at.%) CuNi alloy deposits by characterisation of its morphology and elemental composition as a function of substrate metal (Cu and Ni), charge density, current density, and potential-time response measured during electrodeposition. Alloy deposition starts in favor of Cu, forming a Cu-rich *layer* on a ECD Ni substrate and Cu-rich *islands* on a PVD Cu substrate after which aggregates only form on a Cu substrate, due the ability of BTAH to chemically bond to Cu but not to a Ni surface.

For a controlled growth of binary metal alloys, such as CuNi, the redox potentials of both metal ions should be brought close together. In this and our previous work,[22] we have shown that BTAH is able to both shift the Cu^{2+} reduction potential towards Ni^{2+} reduction onset in the mixed $CuSO_4$ and $NiSO_4$ bath. On Cu substrates and for $CuSO_4$ only bath, the polarization of the BTAH surface layer was such that the potential was shifted even into the HER region. Next to polarization, bond strength of BTAH to the substrate determines the resulting alloy morphology. On a Cu substrate, at which BTAH strongly chemisorbs, CuNi growth initiates at a limited number of hemispherical nuclei which develop into large granules (Fig. 12A). A slightly higher Ni content was detected at the grain boundaries (Fig. 9B). The strong BTAH–Cu bond makes that growth of freshly formed copper nuclei (i.e., initially BTAH-free copper formed during the first potential regime in the transient of Fig. 11A and confirmed with TEM-EDS, Fig. 9) is preferred over further nucleation in the BTAH-surface layer. If the BTAH concentration is high enough, or when BTAH is strongly bonded to the surface (e.g., on Cu oxides), the BTAH-substrate layer will be so effective as a physical barrier layer that deposition only occurs at sites where the metal ions can "break through" the BTAH barrier and a kind of through layer deposition occurs, resulting in islands or dendrites. On a Ni substrate, BTAH adsorption does not play a significant role, resulting in a flatter, somewhat porous, deposit (Fig. 12B). It was further shown that the dynamic adsorption/desorption of BTAH to reach a steady-state coverage on Cu (and CuNi alloys) is slow. Whereas the BTAH surface layer formed on copper substrates under equilibrium is strongly inhibiting kinetics, the adsorption during copper deposition on fresh copper surfaces is slow, explaining the morphological effects. Vice versa, desorption or dilution of already adsorbed BTAH is slow as well. The transient for Cu deposition on BTAH-copper in a BTAH solution took more than 200 s to reach a new steady-state with diluted BTAH coverage (inset in Fig. 11C). This slow BTAH surface interaction led to smooth Cu deposits on a Ni substrate due to differential inhibition of already nucleated copper thus promoting further nucleation, an effect similar to that of suppressor additives in direct plating.[53–55] Vice versa, the opposite differential inhibition effect is observed for Cu (and CuNi) on BTAH–Cu substrates, where growth of fresh copper surface is preferred over further nucleation on the inhibited BTAH–Cu surface. An interesting effect resulting from dynamic BTAH adsorption/ dilution effects was observed on a Ni substrate where in the initial stages of deposition a transition was seen from porous alloy with slow surface adsorption of BTAH to a multilayer with alternating Cu:Ni ratio (Fig. 12B) where the BTAH seems to near its steady-state coverage. On top of these layers there is a transition to granular growth by subsequent nucleation and growth similar to that on copper, albeit with much higher nuclei density and thus less granularity as for Cu deposition on a BTAH-saturated Cu surface. We achieved an acceptable morphology for use in SIC applications, and even though the deposit is not very homogeneous in composition, the Ni content fluctuates between 5 and 10 at.% at the deposit surface which is on target for SIC applications.

Acknowledgments

One of the authors (K.H.) is SB PhD fellow at FWO (project N° 1S64517N) and wishes to acknowledge the Research Foundation Flanders for the financial support of this work.

ORCID

Karel P. S. Haesevoets https://orcid.org/0000-0003-3236-2893
Harold G.G. Philipsen https://orcid.org/0000-0002-5029-1104
Philippe M. Vereecken https://orcid.org/0000-0003-4115-0075

References

1. M. Reber and R. Tielert, *1996 IEEE International Symposium on Circuits and Systems. Circuits and Systems Connecting the World. ISCAS 96*, IEEE, **4**, 121 (1996).
2. R. S. Patti, *Proc. IEEE*, **94**, 1214 (2006).
3. A. W. Topol et al., *IBM J. Res. Dev.*, **50**, 491 (2006).

4. B. Chao, S. H. Chae, X. Zhang, K. H. Lu, J. Im, and P. S. Ho, *Acta Mater.*, **55**, 2805 (2007).
5. B. J. Kim, G. T. Lim, J. Kim, K. Lee, Y. B. Park, H. Y. Lee, and Y. C. Joo, *J. Electron. Mater.*, **39**, 2281 (2010).
6. M. H. Jeong, J. W. Kim, B. H. Kwak, and Y. B. Park, *Microelectron. Eng.*, **89**, 50 (2012).
7. F. Nagano et al., *2017 IEEE International Interconnect Technology Conference (IITC)*, IEEE,**55**, 1 (2017).
8. G. T. Lim, B. J. Kim, K. Lee, J. Kim, Y. C. Joo, and Y. B. Park, *J. Electron. Mater.*, **38**, 2228 (2009).
9. M. O. G. Vakanas, N. Moelans, M. Kajihara, and W. Zhang, *Microelectron. Eng.*, **120**, 133 (2014).
10. H. P. R. Frederikse, R. J. Fields, and A. Feldman, *J. Appl. Phys.*, **72**, 2879 (1992).
11. N. Duan, J. Scheer, J. Bielen, and M. Van Kleef, *Microelectron. Reliab.*, **43**, 1317 (2003).
12. K. J. Rönkä, F. J. J. Van Loo, and J. K. Kivilahti, *Metall. Mater. Trans. A Phys. Metall. Mater. Sci.*, **29**, 2951 (1998).
13. A. Paul, *Thesis*, (TU Eindhoven) (2004).
14. H. Yu, V. Vuorinen, and J. Kivilahti, *IEEE Trans. Electron. Packag. Manuf.*, **30**, 293 (2007).
15. A. Brenner, *Electrodeposition of Alloys* (Elsevier, Amsterdam) ii (1963).
16. W. Shao and G. Zangari, *J. Phys. Chem. C*, **113**, 10097 (2009).
17. K. Popov, P. Zivkovic, and N. Nikolic, *Zast. Mater.*, **57**, 55 (2016).
18. C. Bonhôte and D. Landolt, *Electrochim. Acta*, **42**, 2407 (1997).
19. R. Y. Ying, *J. Electrochem. Soc.*, **135**, 2957 (1988).
20. T. A. Green, A. E. Russell, and S. Roy, *J. Electrochem. Soc.*, **145**, 875 (1998).
21. I. Mizushima, M. Chikazawa, and T. Watanabe, *J. Electrochem. Soc.*, **143**, 1978 (1996).
22. K. P. S. Haesevoets, A. Radisic, and P. M. Vereecken, *J. Electrochem. Soc.*, **166**, D315 (2019).
23. R. Youda, H. Nishihara, and K. Aramaki, *Corros. Sci.*, **28**, 87 (1988).
24. M. Finšgar and I. Milošev, *Corros. Sci.*, **52**, 2737 (2010).
25. F. Grillo, D. W. Tee, S. M. Francis, H. A. Früchtl, and N. V. Richardson, *J. Phys. Chem. C*, **118**, 8667 (2014).
26. F. Grillo, D. W. Tee, S. M. Francis, H. Früchtl, and N. V. Richardson, *Nanoscale*, **5**, 5269 (2013).
27. K. Salorinne, X. Chen, R. Troff W., M. Nissinen, and H. Häkkinen, *Nanoscale*, **4**, 4095 (2012).
28. C. Gattinoni, P. Tsaousis, C. Euaruksakul, R. Price, D. A. Duncan, T. Pascal, D. Prendergast, G. Held, and A. Michaelides, *Langmuir*, **35**, 882 (2019).
29. W. Beckmann, M. Jasner, M. Hecht, and K. Steinkamp, *CuNi 90/10 Piping, the Optimum Material for Seawater Service*, KM Europa Metal Aktiengesellschaft. p. 1 (2001), Osnabruck.
30. F. Grillo, D. W. Tee, S. M. Francis, H. A. Früchtl, and N. V. Richardson, *J. Phys. Chem. C*, **118**, 8667 (2014).
31. Z. Xu, S. Lau, and P. W. Bohn, *Langmuir*, **9**, 993 (1993).
32. B. S. Fang, C. G. Olson, and D. W. Lynch, *Surf. Sci.*, **176**, 476 (1986).
33. J.-O. Nilsson, C. Törnkvist, and B. Liedberg, *Appl. Surf. Sci.*, **37**, 306 (1989).
34. S. L. Cohen, V. A. Brusic, F. B. Kaufman, G. S. Frankel, S. Motakef, and B. Rush, *J. Vac. Sci. Technol. A Vacuum, Surfaces, Film.*, **8**, 2417 (1990).
35. P. G. Cao, J. L. Yao, J. W. Zheng, R. A. Gu, and Z. Q. Tian, *Langmuir*, **18**, 100 (2002).
36. K.-M. Yin and B.-T. Lin, *Surf. Coatings Technol.*, **78**, 205 (1996).
37. N. Zech and D. Landolt, *Electrochim. Acta*, **45**, 3461 (2000).
38. D. Gangasingh, *J. Electrochem. Soc.*, **138**, 3605 (1991).
39. B. V. Tilak, A. S. Gendron, and M. A. Mosoiu, *J. Appl. Electrochem.*, **7**, 495 (1977).
40. E. S. Lambers, C. N. Dykstal, J. M. Seo, J. E. Rowe, and P. H. Holloway, *Oxid. Met.*, **45**, 301 (1996).
41. J. I. Flege, A. Meyer, J. Falta, and E. E. Krasovskii, *Phys. Rev. B - Condens. Matter Mater. Phys.*, **84**, 1 (2011).
42. P. H. Holloway and J. B. Hudson, *Surf. Sci.*, **43**, 123 (1974).
43. G. T. Tyuliev and K. L. Kostov, *Phys. Rev. B*, **60**, 2900 (1999).
44. T. Okazawa, T. Nishizawa, T. Nishimura, and Y. Kido, *Phys. Rev. B - Condens. Matter Mater. Phys.*, **75**, 2 (2007).
45. J. W. Lim, J. Iijima, Y. Zhu, J. H. Yoo, G. S. Choi, K. Mimura, and M. Isshiki, *Thin Solid Films*, **516**, 4040 (2008).
46. J. J. Díaz León, D. M. Fryauf, R. D. Cormia, and N. P. Kobayashi, *Proc. of SPIE*, **9924**, 1 (2016).
47. J. I. Goldstein, D. E. Newbury, P. Echlin, D. C. Joy, C. E. Lyman, E. Lifshin, L. Sawyer, and J. R. Michael, *Scanning Electron Microscopy and X-ray Microanalysis* (Springer, Boston, MA) 3rd ed. (2003).
48. D. C. Joy, *J. Microsc.*, **136**, 241 (1984).
49. R. Shimizu, Y. Kataoka, J. T. Ikuta, T. Koshikawat, and H. Hashimoto, *J. Phys. D: Appl. Phys.*, **9**, 101 (1976).
50. D. R. Lide, *CRC Handbook of Chemistry and Physics* (CRC Press, Boca Raton, FL) 84th ed. 2620 (2003).
51. T. P. Moffat and D. Josell, *J. Electrochem. Soc.*, **159**, D208 (2012).
52. J. K. Nørskov, T. Bligaard, A. Logadottir, J. R. Kitchin, J. G. Chen, S. Pandelov, and U. Stimming, *J. Electrochem. Soc.*, **152**, J23 (2005).
53. M. Nagar, A. Radisic, K. Strubbe, and P. M. Vereecken, *ECS Trans.*, **41**, 99 (2019).
54. P. M. Vereecken, A. Radisic, and F. M. Ross, *J. Electrochem. Soc.*, **166**, D3129 (2019).
55. A. Radisic and P. M. Vereecken, *Copper Electrodeposition for Nanofabrication of Electronics Devices, Nanostructure Science and Technology.*, ed. K. Kondo, R. N. Akolkar, D. P. Barkey, and M. Yokoi (Springer, New York, NY) 131 (2014).